

See discussions, stats, and author profiles for this publication at: <https://www.researchgate.net/publication/337117161>

# Design Principles for Central Pattern Generators With Preset Rhythms

Article in IEEE Transactions on Neural Networks and Learning Systems · November 2019

DOI: 10.1109/TNNLS.2019.2945637

CITATIONS

24

READS

191

3 authors:



**Matteo Lodi**

Università degli Studi di Genova

44 PUBLICATIONS 285 CITATIONS

SEE PROFILE



**Andrey Shilnikov**

Georgia State University

216 PUBLICATIONS 4,163 CITATIONS

SEE PROFILE



**Marco Storace**

Università degli Studi di Genova

192 PUBLICATIONS 1,948 CITATIONS

SEE PROFILE

Some of the authors of this publication are also working on these related projects:



Analysis and Exploration of Deterministic chaos [View project](#)



Analysis and Design of Central Pattern Generators [View project](#)

# Design Principles for Central Pattern Generators With Preset Rhythms

Matteo Lodi<sup>1</sup>, Andrey L. Shilnikov, and Marco Storace<sup>2</sup>, *Senior Member, IEEE*

**Abstract**—This article is concerned with the design of synthetic central pattern generators (CPGs). Biological CPGs are neural circuits that determine a variety of rhythmic activities, including locomotion, in animals. A synthetic CPG is a network of dynamical elements (here called cells) properly coupled by various synapses to emulate rhythms produced by a biological CPG. We focus on CPGs for locomotion of quadrupeds and present our design approach, based on the principles of nonlinear dynamics, bifurcation theory, and parameter optimization. This approach lets us design the synthetic CPG with a set of desired rhythms and switch between them as the parameter representing the control actions from the brain is varied. The developed four-cell CPG can produce four distinct gaits: walk, trot, gallop, and bound, similar to the mouse locomotion. The robustness and adaptability of the network design principles are verified using different cell and synapse models.

**Index Terms**—Bifurcation analysis, central pattern generators, neuronal models, parameter optimization.

## I. INTRODUCTION

CENTRAL pattern generators (CPGs) for locomotion are [small] neural networks able to produce rhythmic outputs even in the absence of sensory feedback or higher motor planning centers inputs [1]–[4]. CPGs are studied at the crossroad between many diverse disciplines including biology, neuroscience, robotics, nonlinear dynamics, biomechanics, to name a few. Each discipline deals with this common topic using different tools and by pursuing different goals: knowing their physiological structure, understanding their functional roles, reproducing their functional mechanisms in developed mathematical models, or exploiting them in robotics or neuroprosthetics applications. Biological CPGs of most vertebrates are composed of a large number of coupled neurons, which can be subdivided into smaller clusters or cohorts that behave coherently. Therefore, the orchestrated activity of each cluster can be modeled as if it was produced by a single neuron.

Manuscript received July 16, 2018; revised April 8, 2019; accepted October 1, 2019. Date of publication November 8, 2019; date of current version September 1, 2020. This work was supported in part by the University of Genoa. The work of A. L. Shilnikov was supported in part by the NSF under Grant IOS-1455527 and in part by the Russian Science Foundation (RSF) through the Lobachevsky University of Nizhny Novgorod under Grant 14-41-00044. (*Corresponding author: Marco Storace.*)

M. Lodi and M. Storace are with the Department of Electrical, Electronic, Telecommunications Engineering and Naval Architecture, University of Genoa, 16145 Genoa, Italy (e-mail: marco.storace@unige.it).

A. L. Shilnikov is with the Department of Mathematics and Statistics, Neuroscience Institute, Georgia State University, Atlanta, GA 30303 USA.

Color versions of one or more of the figures in this article are available online at <http://ieeexplore.ieee.org>.

Digital Object Identifier 10.1109/TNNLS.2019.2945637

Such a cluster is termed in many ways: a neural population, a unit, a building block, or a cell—the term that we adopt in this article. The cells are connected by synapses to create the CPG.

In this article, we focus on models of CPGs that determine and control the locomotion of quadrupeds. In particular, we discuss a set of operating principles that are employed in our design of synthetic CPGs to reproduce a number of prescribed gaits specific for the mouse locomotion. Our goal is to derive design rules for the multi-functional CPGs that can produce distinct mouse gaits and smooth transitions between them, depending on some drive or bifurcation parameter. Such a parameter can represent a control action from the brain or, more precisely, the brainstem control throughout neurons acting as key intermediaries between higher motor planning centers and CPGs [11]–[13]. Our approach to model motor CPGs is based on the theory of dynamical systems [5], [6], which is well suited for understanding a multiplicity of nonlinear recurrent oscillations, their stability conditions, and bifurcations that can occur in such small rhythm-generating neural networks [7]–[10]. Previously, we proposed the computational toolkit CEPAGE [15] to analyze dynamics and bifurcations in simple CPGs emulating quadruped (mouse) locomotion as the control parameter is varied [14], [16]. Here, we present an advanced four-cell CPG model that more phenomenologically fits biological CPGs governing quadruped locomotion, being able to generate four different gaits: walk, trot, gallop, and bound. We also discuss minimal operating principles as well as generic properties, the adopted models of cells and synapses should meet to ensure the robustness and structural stability of the desired CPG functions.

In summary, in this article we: 1) point out the qualitative properties that the cell and synapse models must be endowed with to meet the design goals; 2) define a sequence of steps to design a reduced multifunctional CPG model producing several rhythms and switch between them smoothly with variations of the control parameter; and 3) demonstrate that our design approach is quite robust with respect to the choice of synapse and cell models.

The rest of this article is organized as follows. Section II introduces the main features of the developed CPG. Section III presents in detail the proposed know how to design a synthetic CPG with preset rhythms. In Section IV, we verify the robustness of the proposed design with respect to changes in its components (models). Finally, Section V draws some conclusions.

## II. BASIC ELEMENTS

In this section, we summarize the pivotal elements of the proposed CPG design approach.

### A. Cell

Our primary goal is better understanding the functional mechanisms underlying rhythmogenesis in biological CPGs. Therefore, our description of any cell in this article is not meant to provide a 1:1 correspondence to a synchronous group of neurons, but rather a macromodel for several groups of interneurons functioning together, like half-center oscillators, for example. In other words, our CPG models have a level of abstraction higher than usual. In this perspective, the hierarchical structures often adopted to represent CPGs [17] or the functional subnetwork approach proposed in [18] can be hardly compared to our neural circuits as the CPGs designed according to the former approaches have a finer granularity, i.e., they contain a larger number of cells than our reduced models. The activity of the generic  $i$ th cell is revealed through a variable representing its membrane voltage  $V_i(t)$ .

### B. Phenomenological Design Outline

Rhythmic movements in animals result from the interplay between the sensory system (sensor), the musculoskeletal system (actuator), and the neural system (control). The neural system, in particular, performs three main control actions [3]. The first, open-loop control action is provided at the level of the spinal cord by the CPG generating the given pace; these neural networks include half-center oscillators—a pair of neural populations reciprocally coupled by inhibitory synapses that autonomously oscillate in alternation [19], [20]. The second, closed-loop control action is provided by a sensory-driven feedback, which provides information about the mechanical interaction of the animal body with the environment and secures adaptation to unexpected obstacles and uncertainties during ambulatory excursions. The third, also called closed-loop control action is ensured by supra-spinal networks, which, based on sensory information (usually, mainly visual and tactile), timely inform the CPG about the rhythm (and corresponding gait) to be imposed, thus changing muscle activity. Here, we consider only the first and part of the third control actions.

The reciprocal interactions of these basic mechanisms concur to the interlimb coordination and produce flexible and efficient locomotion. The detailed biophysical mechanisms underlying locomotion are yet to be fully understood. Therefore, the current research focusing on the phenomenologically reduced CPG design (oriented toward robotic applications) pursues several development lines based on decentralized control [21], bottom-up approach with the use of functional blocks [18], nonlinear dynamics, and bifurcation theory [16], [22].

### C. Effective Variables and Parameters

The existence and stability of rhythmic patterns generated by CPGs are analyzed using the so-called phase lags

TABLE I

GAITS CHARACTERISTICS: FREQUENCY ( $f$ ), DC, PHASE-LAGS BETWEEN LEGS AND CORRESPONDING  $\alpha$ -VALUES

Gait	$f$ [Hz]	$dc$	LF-RF ( $\Delta_{12}$ )	LF-LH ( $\Delta_{14}$ )	LF-RH ( $\Delta_{13}$ )	$\alpha$
W	[2, 4]	< 0.4	0.5	0.25	0.75	[0, 0.25]
T	[4, 9]	[0.4, 0.51]	0.5	0.5	0	[0.25, 0.5]
G	[9, 10]	> 0.51	0.1	0.6	0.5	[0.5, 0.75]
B	[10, 12]	> 0.51	0	0.5	0.5	[0.75, 1]

introduced for oscillatory or bursting cells [7], [24], [25]. All isolated/coupled cells are assumed to have and maintain relatively close temporal characteristics. In the dynamical systems terminology, this means that each  $i$ th cell resides on a structurally stable periodic orbit of period  $T_i$  in the state space of the corresponding model. Its current position on the periodic orbit can be determined using a new phase variable  $\phi_i(t) \in [0, 1)$ , defined modulo 1, such that  $\phi_i$  is reset to 0 when the voltage  $V_i$  increases above some synaptic threshold  $V_{th}$  at times  $t_i^{(k)}$ . The phase-lag representation of an  $N$ -cell network employs  $N - 1$  state variables describing the phase lags  $\Delta_{1i}(t) = \phi_i(t) - \phi_1(t)$  between the spike/burst initiations in the reference cell 1 and the other ones coupled within the network. The time evolutions of these state variables, being quite complex due to nonlinear interactions, can be determined through numerical simulations. For that purpose, we compute the phase lags between coupled cells in a discrete set of time instants as

$$\Delta_{1i}^{(k)} = \frac{t_i^{(k)} - t_1^{(k)}}{t_1^{(k)} - t_1^{(k-1)}}, \quad \text{mod } 1. \quad (1)$$

As time progresses, the phase lags  $\Delta_{1i}^{(k)}$  can converge to a single or several steady or phase-locked states. The presence of multistability can be evidenced by integrating the system of equations governing the network densely sweeping initial conditions for phases.

The locomotion in quadrupeds is produced by the coordination of limbs movements with specific speed (frequency) and ratio between the stance and swing phase [duty cycle (DC)] and with the given phases in the repetitive patterns that drive the limbs. The coordination, i.e., the specific phase lags between the limbs, determines the animal gait, which usually changes with the speed. This modeling paper is focused on the locomotion of mice, which can exhibit four different gaits: walk (W), trot (T), gallop (G), and bound (B), with frequency  $f$  and DC ranging in the intervals [2, 12] Hz and [0.25, 0.6], respectively [27], [28]. Table I summarizes the characteristics of mouse gaits, extracted from [27] and [28]. Assuming that the CPG contains one cell per leg with L = left, R = right, F = fore, and H = hind, we take as reference leg LF and compute the phase lags LF-RF ( $\Delta_{12}$ ), LF-LH ( $\Delta_{14}$ ), and LF-RH ( $\Delta_{13}$ ).

At low speed ( $f < 4$  Hz), mice walk: in this gait, the swing phase is shorter than the stance phase and the limbs swing one at a time. Trot occurs at medium speed ( $4 < f < 9$  Hz): in this gait, the stance and swing phases have the same duration, left–right, and fore–hind limbs move in alternation.

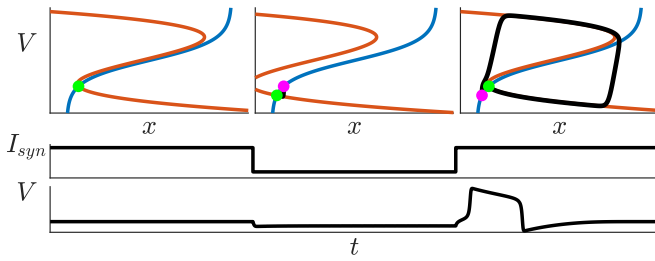


Fig. 1. Postinhibitory rebound mechanism in  $B$ -model with the parameters listed in Appendix A, except  $g_D = 0$ . Top: postinhibitory trajectory (black line) in the phase space superimposed with the fast  $V$ - and slow  $x$ -nullclines (orange and blue, respectively) crossing at the equilibrium state (green dot). Application of negative pulse (middle) causes first hyperpolarization followed by the postinhibitory rebound in the cell voltage (bottom).

Gallop is exhibited at medium–high speeds ( $9 < f < 10$  Hz): in this gait, the swing phase is slightly longer than the stance phase, left and right limbs move almost together, whereas fore and hind limbs move in alternation. At high speed ( $f > 10$  Hz) mice bound: in this gait, the swing phase is again slightly longer than the stance phase, fore and hind limbs move in alternation, whereas left and right limbs move together.

Sequential switching from one gait to another is controlled by the bifurcation parameter  $\alpha \in [0, 1]$ , which represents the control action provided by supra-spinal networks: the mouse speed increases with increasing  $\alpha$  values. The transitions between these gaits occur sequentially as the parameter is increased/decreased; we chose to assign one-quarter of the parameter range to each gait.

### III. PROPOSED METHOD

In this section, we propose a sequence of operating principles and steps to design a reduced CPG circuit producing a desired set of gaits.

#### A. Choice of the Cell Model: The PIR Mechanism

In the design of a synthetic CPG, a proper understanding of its biological functions helps one to optimize the tradeoff between the unavoidable complexity of biological phenomena and the necessary simplicity of mathematical modeling. Therefore, the models employed in this article have to possess the mechanism reproducing the so-called postinhibitory rebound (PIR) of the cell membrane voltage, which occurs as soon as the postsynaptic quiescent cell is abruptly released from hyperpolarizing inhibition (e.g., due to an external current pulse) or from another presynaptic cell of the network. The PIR mechanism allows two reciprocally inhibiting cells to generate self-sustained oscillations [19], [29]. In particular, in a half-center oscillator made of two cells coupled reciprocally with fast inhibitory synapses, this mechanism lets the half-center oscillator generate self-sustained spiking/bursting in alternation. This effect is qualitatively illustrated in Fig. 1 for an isolated cell described by model B in Appendix A. The model has two dynamic variables,  $V$  and  $x$ , representing the fast voltage and slow gating variables, respectively. The top of

Fig. 1 shows the  $(x, V)$ -phase portrait with the fast  $Z$ -shaped nullcline (orange line) on which  $\dot{V} = 0$  and the slow nullcline (blue line) on which  $\dot{x} = 0$ . Their only intersection point to the right of the knee on the low branch of the  $V$ -nullcline is a stable equilibrium state (marked as the green dot) of the model, corresponding to the quiescent hyperpolarizing state of the cell. Due to the slow–fast nature of the model, its solutions converge to this state following the shape of the fast nullcline. The negative pulse of external current  $I_{syn}$ , leaving the  $x$ -nullcline intact, makes the  $V$ -nullcline shift to the left so that the stable equilibrium state of the unperturbed system (marked by the purple dot in the top-central panel) moves below and to the left (green dot) in the  $V$ -nullcline of the perturbed system. Correspondingly,  $V(t)$  drops down (bottom). We note that the PIR-mechanism requires three necessary conditions be met: the hyperpolarizing perturbation, due to either an external pulse or the inhibitory current, must be: 1) strong; 2) long enough; and 3) must have a rapid termination phase. This means that the ascending front of the pulse must be nearly vertical as one shown in the middle in Fig. 1, and the synapse must be fast, not slow. After  $I_{syn}$  is abruptly turned off, the state  $(x, V)$  starts from the position of the disappeared equilibrium point (purple dot in the top right), follows the upper and lower branches of the  $V$ -nullcline and converges back to the original equilibrium point (green dot), and tracing down a transient excursion (black thick trajectory in the top right) corresponding to the outburst in the voltage trace (bottom).

In our CPG model, a cell is described by the following state equation:

$$\dot{\mathbf{z}}_i = \begin{bmatrix} \dot{V}_i \\ \dot{\mathbf{x}}_i \end{bmatrix} = \begin{bmatrix} f_i(\mathbf{z}_i, I_{syn}^{(i)}(\alpha), g_D D_i(\alpha)(V_i - E)) \\ \mathbf{p}_i(\mathbf{z}_i) \end{bmatrix} \quad (2)$$

where  $V_i$  is treated as the membrane potential of the  $i$ th cell, while  $\mathbf{x}_i$  represents its gating variables and  $I_{syn}^{(i)}$  is its incoming synaptic current. The term  $g_D D_i(\alpha)(V_i - E_{ex})$  describes an overall influence (modulated through the  $\alpha$ -parameter) of the supraspinal networks on the given postsynaptic cell.

To examine and tune up the CPG outcomes, in this article, we adopt three models of its cells that all exhibit the PIR. These are the conductance-based model used in [30] (code-named model A), a generalized FitzHugh–Nagumo model [8] (model B), and the adaptive exponential integrate-and-fire model [31] (model C) that can also generate bursting activity. They are described in Appendix A.

#### B. Choice of the Synapse Model

The synapses in our CPG models are required to demonstrate a rapid time course [20]. Here, we consider three models of such fast synapses: the first two ones are represented by the fast threshold modulation (FTM) synapses [32], with different activation functions, namely, given by the sigmoidal (model  $\beta$ ) and stepwise (model  $\gamma$ ) functions; the third model is the dynamical  $\alpha$ -synapse (model  $\delta$ ) [19], [33], which, in general, is not necessarily fast.

In a CPG composed of  $N$  cells, we introduce the action of inhibitory, excitatory, and delayed inhibitory chemical

synapses on the  $i$ th cell as follows:

$$I_{\text{syn}}^{(i)}(\alpha) = \sum_{j=1}^N \left\{ g_{ij}^{\text{in}} A(V_j(t), s_{\text{in}}(t))(E_{\text{in}} - V_i(t)) \right. \\ \left. + g_{ij}^{\text{di}} A(V_j(t - \tau), s_{\text{di}}(t))(E_{\text{in}} - V_i(t)) \right. \\ \left. + g_{ij}^{\text{ex}}(\alpha) A(V_j(t), s_{\text{ex}}(t))(E_{\text{ex}} - V_i(t)) \right\} \quad (3)$$

where  $I_{\text{syn}}^{(i)}$  is the current injected into the  $i$ th cell,  $V_i$  and  $V_j$  are the membrane potentials in the post and presynaptic cells, respectively,  $s_{\text{xx}}$  is the synapse state (only for dynamical synapses),  $g_{ij}^{\text{xx}}$  is the maximal synapse strength,  $A(V_j, s_{\text{xx}})$  is the synapse activation function ( $A$  depends on the state only for dynamical synapses),  $E_{\text{xx}}$  is the synapse reverse potential, and  $\tau$  is the synapse delay; here, *in*, *di*, and *ex* stand for inhibitory, delayed inhibitory, and excitatory, respectively.

We note that, as described in Section III-C, the weights of the excitatory synapses vary with changes in  $\alpha$  values to reproduce the effect of the brainstem on the excitatory interneuron populations in a real CPG.

### C. Network Assembly Line: Operating Principles

Our network governing the mice locomotion results from a reduction of the 40-cell CPG proposed in [30] to regulate both speed and gaits of the mouse. The 40-cell CPG is made of four blocks of rhythm-generators (RGs), each driving a limb, that are all cross-linked through inhibitory and excitatory interneuron populations. Each RG contains two populations, flexor and extensor, which inhibit each other and control the swing and stance phases of the limbs. In particular, when the flexor (extensor) population is active, the corresponding limb is in the swing (stance) phase. The gait generated by the CPG can be controlled through variations of  $\alpha$ .

To simplify the 40-cell CPG, we employ the strategies proposed in [14] and [16], which can be summarized in three steps: 1) substitute the interneuron populations with fast chemical synapses, inhibitory or excitatory, depending on the nature of the replaced population; 2) remove the extensor populations; swing phase is still regulated by the flexor units, whereas the stance phase is activated when the flexor units are silent; and 3) add inhibitory delayed synapses between left and right cells to reproduce the action of extensor populations.

We remark that step A can be achieved using several inhibitory pathways, as shown in Fig. 2. In particular, the simplified two-cell circuit shown in Fig. 2(c) can model both the inhibitory pathways shown in Fig. 2(a) and (b), which are commonly found in biological neural circuits [34], [35]. The resulting simplified CPG circuit is shown in Fig. 3(a). It contains four numbered cells only, each one driving a particular limb, labeled as follows: L = left, R = right, H = hind, and F = fore. They are cross connected with fast inhibitory (gray), excitatory (black), and delayed inhibitory (orange) synapses. An equivalent yet compact notation for the circuit is presented in Fig. 3(b). The circuit in Fig. 3 has a general structure that might represent not only a simplified biologically inspired CPG but also some generic synthetic CPG (with only homolateral and commissural connections) with four

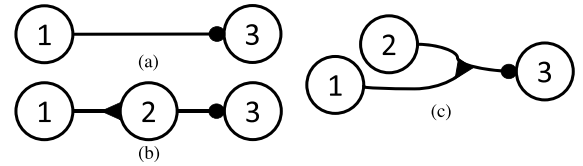


Fig. 2. Reduced circuit (a) representing two typical inhibitory 3-cell pathways where either cell 1 first excites the middle cell 2 that next inhibits cell 3 (b), or excitatory cell 1 facilitates the inhibition projected from cell 2 onto the postsynaptic cell 3 (c). Inhibitory and excitatory synapses are marked by circle  $\bullet$ - and triangle  $\Delta$ -shaped terminals, respectively.

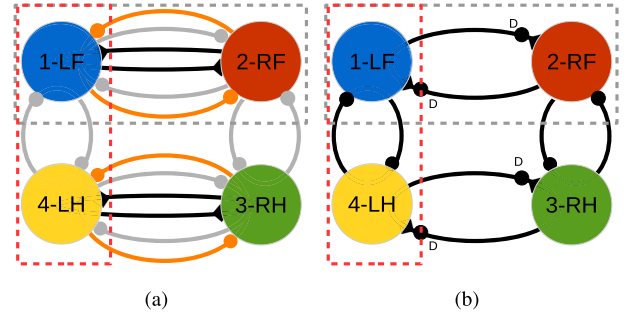


Fig. 3. Proposed 4-cell CPG to govern the mouse locomotion, with (a) complete and (b) compact circuitry. The four numbered cells are cross-connected with synapses: fast inhibitory [marked by gray/black dots  $\bullet$  in (a) and (b)], delayed inhibitory [orange dots in (a) and marked with  $D$  i (b)], and excitatory (black triangles  $\Delta$ ).

cells to regulate limb flexors in quadrupeds. Similar spatio-symmetric circuits have been identified in various biological CPGs, including swim CPGs in the mollusks *Melibe leonina* and *Dendronotus iris* [36]–[38]. In other words, the CPG topology can be either bioinspired or assigned/decided by the designer.

### D. Parameter Selection Strategy

We describe our parameter selection strategy by employing the same cell and synapse models as in [14]. This allows us to both illustrate our design method and validate the obtained results by comparison with this benchmark.

Once the CPG topology is defined (either by simplifying a bioinspired model or by making direct reference to a structure relying on symmetry properties), we first have to choose which CPG parts depend on the  $\alpha$  parameter. In the case of bioinspired architectures, this information can be simply inferred from the original CPG. For synthetic CPGs, we can follow two guidelines: 1) all cells have to depend on  $\alpha$ , in order to make frequency and DC  $\alpha$ -dependent and 2) about synapses, we assume as  $\alpha$ -dependent those that allow us to break symmetries, thus enabling gait transitions. Of course, more refined strategies could be used: for instance, one can decide that *a priori* all synapses depend on  $\alpha$  and then check *a posteriori* which connections show an effective dependence on the brainstem control. The price to be paid would be an increase in the computational costs. This is an open problem, and the solution proposed here is a tradeoff between computational complexity in the design phase and the accuracy of the obtained model.

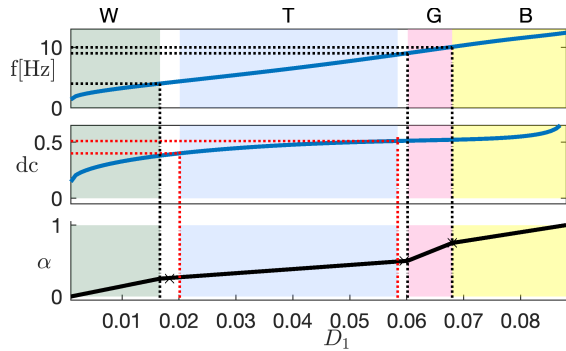


Fig. 4. Frequency  $f$  (top) and DC (middle) plotted against the driving function  $D_1(\alpha)$  of the control parameter  $\alpha$  (bottom). Dotted lines: boundaries for each gait (see Table I). Crosses: landmarks used to define the function  $D_1(\alpha)$ . White regions: coexisting stable gaits.

Summing up, in our case-study, we assume that all cells [through the function  $D_i(\alpha)$ ] and all excitatory synapses [through the strengths  $g_{ij}^{\text{ex}}(\alpha)$ ] depend on  $\alpha$ , as pointed out in (2) and (3), whereas we fix the inhibitory synapses strengths  $g_{ij}^{\text{in}}$  and  $g_{ij}^{\text{di}}$  to the values listed in Appendix B.

For the sake of simplicity, we assume that the functions  $D_i(\alpha)$  and  $g_{ij}^{\text{ex}}(\alpha)$  are piecewise linear (PWL). We calibrate these functions in order to make our CPG able to produce all gaits listed in Table I. To this end, we make the following steps, with the aid of the computational toolbox CEPAGE [15].

*Step 1 [Clock Tuning (Acting on the Fore Cells)]:* Let us focus on reference cell 1 isolated from the rest of the CPG. We first assess frequency  $f$  and DC of the state variable  $V_1(t)$  for a range of  $D_1$ -values. For instance, the bifurcation diagram shown in Fig. 4 is built on a 1-D 100-long array of equidistant  $D_1$ -values. We remark that  $D_1$  influences the behavior of cell 1, according to (2) and (4). The  $D_1$  range is chosen so that the cell is not quiescent. The figure illustrates how the frequency  $f$  (top) and the DC (middle) of the generated membrane voltage  $V_1(t)$  vary as  $D_1$  is increased. These plots (numerically obtained using the CEPAGE package) are used to identify the  $D_1$  ranges corresponding to different gaits according to Table I. For instance, the green region corresponds to walk, as in the  $D_1$  range  $[0, 0.017]$ , the frequency range is  $[2, 4]$  Hz and DC remains below 0.4. The same holds for the other colored regions.

Next, we choose the monotonically increasing PWL function  $D_1(\alpha)$  passing through a set of selected landmarks. The PWL function  $D_1(\alpha)$  is chosen so that, while  $\alpha$  increases from 0 to 1, both  $f$  and DC increase monotonically between their minimum and maximum values given in Table I:  $f$  ranges between 2 and 12 Hz, whereas DC varies between 0.25 and 0.65. To this end, we set some landmarks on the plane  $(D_1, \alpha)$  (bottom): we chose to set them at the transitions between the gaits, imposing that these transitions happen at the values  $\alpha = 0.25, 0.5, 0.75$ , according to Table I. The PWL function  $\alpha(D_1)$  (black thick curve) is a mere linear interpolation of these landmarks and its inverse is the desired function  $D_1(\alpha)$ . Finally, we set  $D_2(\alpha) = D_1(\alpha)$ , as cell 2 (when isolated) is identical to cell 1. Through this step, we exploit brute-force

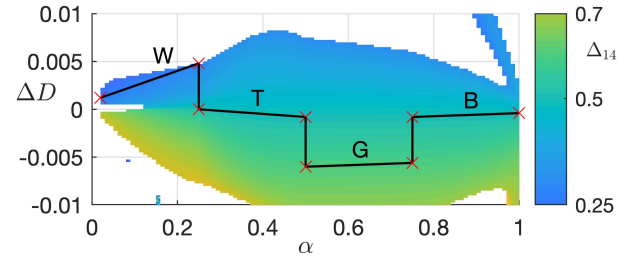


Fig. 5. Bifurcation diagram in the  $(\alpha, \Delta D)$ -parameter plane. It is color-mapped according to the values of the phase-locked lag  $\Delta_{14}$  (vertical bar on the right). The CPG is silent in the white regions and generates rhythmic outcomes in the color regions. Red crosses: landmarks used to define the function  $\Delta D(\alpha)$  (PWL black line).

bifurcation analysis to establish a direct dependence of  $f$  and DC for the fore cells on  $\alpha$ , by properly defining the PWL function  $D_1(\alpha)$ , which influences the cell dynamics, according to (2).

*Step 2 [Fore-Hind Coordination (Acting on the Hind Cells)]:* Now, we consider the neural circuit within the dashed red rectangle in Fig. 3 and set  $D_4(\alpha) = D_1(\alpha) + \Delta D(\alpha)$ . Next, we perform the bifurcation analysis to find the PWL function  $\Delta D(\alpha)$ , which ensures the desired synchronization between cells 1 and 4, i.e., between the hind and fore limbs. To this end, we obtain a brute-force 2-D bifurcation diagram by plotting the asymptotic phase-lag  $\Delta_{14}$  for a grid of values of  $\Delta D$  and  $\alpha$ . For instance, the bifurcation diagram in Fig. 5 corresponds to a 2-D  $(\alpha, \Delta D)$ -parameter sweep on a uniform  $200 \times 200$ -grid of the parameter values. In the white regions, the CPG does not oscillate, as cells 1 and/or 4 remain inactive. In the colored region,  $\Delta_{14}$  varies in the range  $[0.25, 0.7]$ . This means that the left-hand side half-center oscillator made of cells 1 and 4 (which is in charge of the front-hind synchronization) can exhibit a great capacity of asymptotic phase-locked states, which, in turn, ensures a large variability in the gaits. Next, we define the function  $\Delta D(\alpha)$  so that it passes through a set of selected points, on the  $(\alpha, \Delta D)$ -sweep diagram. To select the landmarks (indicated by red crosses in Fig. 5), we focus again on the transitions between different gaits. For instance, the walk gait corresponds to  $\Delta_{14} = 0.25$  (see Table I). Therefore, we place two landmarks with  $\alpha$  coordinates 0 and 0.25 (bounds of the walk gait, see Table I) and  $\Delta D$  coordinates corresponding to dark blue pixels, i.e., to the phase-locked lag LF-LH  $\Delta_{14} = 0.25$ . Moreover, in order to ensure that the gait is maintained within the whole  $\alpha$ -interval, we choose the two landmarks such that the connecting segment lies over dark blue pixels. By following the same line of reasoning for all gaits, we define  $\Delta D(\alpha)$  as the PWL function connecting the landmarks, as shown (black line) in Fig. 5: the PWL curve stays within the color regions in the parameter space and each segment of  $\Delta D(\alpha)$  corresponds to a specific gait (corresponding to a color) occurring within the given  $\alpha$ -window. Finally, we set  $D_3(\alpha) = D_4(\alpha)$  in virtue of the network symmetry.

*Step 3 [Left-Right Coordination (Acting on the Synapses)]:* In this step, we tune up the neural circuit singled out within

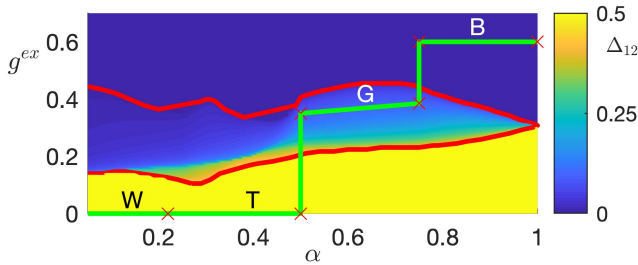


Fig. 6. Bifurcation diagram in the  $(\alpha, g^{\text{ex}})$ -parameter plane, color-mapped according to the values of the phase-locked lag  $\Delta_{12}$  (vertical bar on the right). Landmarks (red crosses) are used to define the PWL function  $g^{\text{ex}}(\alpha)$  (green curve).

the dashed gray rectangle in Fig. 3 and set  $g_{21}^{\text{ex}}(\alpha) = g_{12}^{\text{ex}}(\alpha) = g^{\text{ex}}(\alpha)$  (strength of the black synapses), as there is experimental evidence [3] that the brainstem control acts in the same way on the synapses connecting cells 1–2 and 3–4. As for the previous steps, the PWL function  $g^{\text{ex}}(\alpha)$  is defined by exploiting bifurcation analysis, in order to ensure the desired synchronization between left and right cells. First, we find the phase-locked lag  $\Delta_{12}$  for an array of values of  $g^{\text{ex}}$  and  $\alpha$  to get another brute-force 2-D bifurcation diagram. Fig. 6 shows the results of a 2-D  $(\alpha, g^{\text{ex}})$ -parameter sweep on a uniform  $200 \times 200$ -grid for our case study. In the top part of the bifurcation diagram (dark blue region), the cells synchronize in-phase ( $\Delta_{12} = 0$ ), whereas in the bottom part (yellow region), they synchronize in antiphase ( $\Delta_{12} = 0.5$ ), according to the color-bar for the phase-lag  $\Delta_{12}$  on the right-hand side. In the central region, marked with two red curves, the network becomes bistable and can generate two distinct rhythmic patterns. This bistability is due to two pitchfork bifurcations, forward and backward, occurring at the parameter values marked by the red lines, found with a brute-force numerical analysis through CEPAGE. In this bistability region, there are two stable equilibrium states: one associated with the phase-coordinate  $0 \leq \Delta_{12} \leq 0.5$ , and its mirror-image with phase  $(1 - \Delta_{12})$ .

Finally, we define the function  $g^{\text{ex}}(\alpha)$  so that it passes through a set of landmarks in the found bifurcation diagram. Just to set the ideas (the gait order is unessential, in this step), we start calibrating the CPG circuit so that it can produce the bound gait, with the desired phase-locked lags LF-RF (see Table I). This gait requires  $\Delta_{12} = 0$ , and therefore, the range of the driving function  $g^{\text{ex}}(\alpha)$  must lie within the dark blue region in Fig. 6. For simplicity, we pick  $g^{\text{ex}}(\alpha) \simeq 0.6$  for  $0.8 \leq \alpha \leq 1$ . Next, we select  $g^{\text{ex}}(\alpha) = 0$ , for  $0 \leq \alpha \leq 0.5$ , corresponding to the walk and trot gaits, characterized by  $\Delta_{12} = 0.5$ . Finally, for the gallop at the mid speed, we select a set of landmarks (red crosses) yielding  $\Delta_{12} \simeq 0.1$  in the central region of the bifurcation diagram. On the whole, the function  $g^{\text{ex}}(\alpha)$  is the PWL green curve shown in Fig. 6.

Using the same strategy, we can independently calibrate the subnetwork controlling the phase lag LH-RH  $\Delta_{34}$  by selecting the corresponding PWL functions  $g_{34}^{\text{ex}}(\alpha) = g_{43}^{\text{ex}}(\alpha)$ . The results are completely similar [even if not equal,

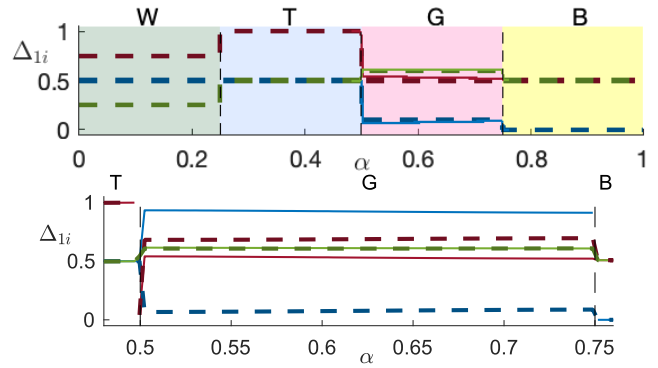


Fig. 7. Top: desired (dashed lines) and simulated (solid lines) phase-locked lags  $\Delta_{1i}$ , with  $i = 2$  (blue lines),  $i = 3$  (red lines) and  $i = 4$  (green lines), plotted versus  $\alpha$ . The colors evidence the existence windows corresponding to the four gaits: walk, trot, gallop and bound. Bottom: enlargement with  $\alpha \in [0.475, 0.775]$  demonstrating bistability for the gallop gait due to the forward and backward pitchfork bifurcations that give rise to two possible asymptotic phase-lag  $\Delta_{1i}$  (shown as dashed and solid lines), for  $i = 2$  (blue) and  $i = 4$  (red). For  $i = 3$  (green) there is only one steady-state phase-lag.

as  $D_1(\alpha) \neq D_3(\alpha)$ ] to those found in Fig. 6 and, hence, are not discussed here for the sake of conciseness.

*Step 4 [Complete CPG (a posteriori Validation)]:* Since the previous steps, acting locally, do not fully guarantee that the complete CPG dynamics is as desired, in the last step we need to verify the overall CPG behavior. To do that, we simulate the CPG performance by employing the PWL function selected in the previous steps for a grid of values of  $\alpha$  and we compare the obtained asymptotic phase lags with the values in Table I.

Fig. 7 (top) shows the desired (dashed lines) phase-locked lags  $\Delta_{1i}$  from Table I plotted against the control parameter  $\alpha$  for our case study:  $\Delta_{12}$  (blue lines),  $\Delta_{13}$  (red lines), and  $\Delta_{14}$  (green lines), between the cells of the CPG. They overlap almost everywhere with the simulated ones (solid lines) for all four gaits: walk, trot, gallop, and bound. One can easily verify that the phase lags meet the requirements (legs' movements) described in Section II-C: for instance, in the walk gait, the four cells activate sequentially in the order 1–4–2–3, as shown in the top of Fig. 8.

As we pointed out above, at the transitions from trot to gallop and from gallop to trot, two pitchfork bifurcations occur. This causes the effect of bistability in the gallop region, as magnified in the bottom of Fig. 7. Both stable equilibrium states in the 3-D  $(\Delta_{12}, \Delta_{13}, \Delta_{14})$ -phase space of the network system correspond to the same gallop gait, though with reverse order of moving limbs.

To check that the CPG switches smoothly between gaits, Fig. 8 shows the time evolution of the membrane voltages  $V_i$  and of the phase-lags  $\Delta_{1i}$  of the network when  $\alpha$  is increased smoothly across the edge between: walk and trot (top), trot and gallop (middle), and gallop and bound (bottom). It is apparent (from both the time and phase-lag plots) that all gait transitions are smooth.

In summary, the original CPG circuit can be effectively reduced at the cost of a reasonable complication of the synaptic connectivity. The desired gaits are achieved by affecting

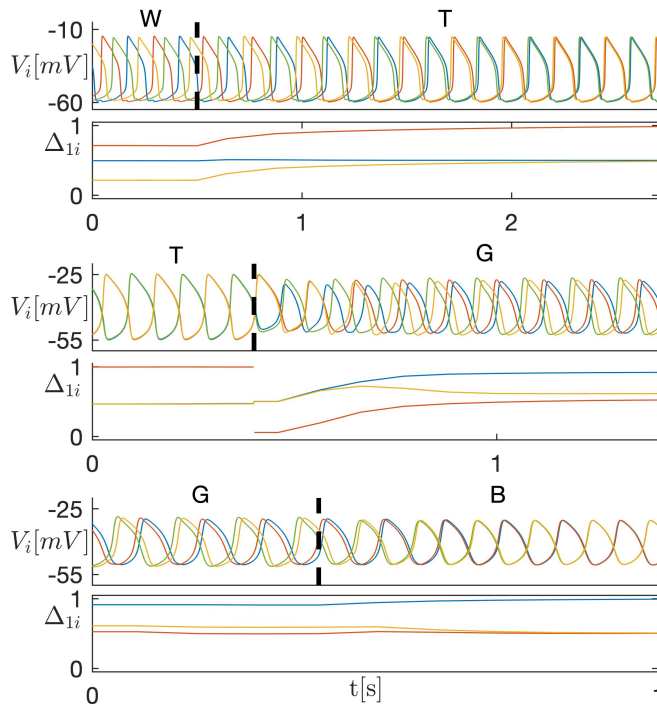


Fig. 8. Time-plots of the “membrane potentials”  $V_i$ , and phase-lags  $\Delta_i$ , at gait transitions: from walk to trot (top), from trot to gallop (middle), and from gallop to bound (bottom). The colors of the  $V_i(t)$  curves are matched with those of the corresponding cells in Fig. 3.

the reference cell and its synaptic connections with other cells of the network. The synaptic strengths and each cell model depend on the single control parameter  $\alpha$ . The specific profiles of these dependencies are chosen through a design strategy based on the methods of nonlinear dynamics and bifurcation analysis. The network symmetry allows us to use many simplifications to calibrate the CPG step-by-step, first at the cellular and further at the network level. We set the reference cell (here 1) to define the dependence of the frequency  $f$  and DC on the single control parameter  $\alpha$ . Then, we find the conditions to maintain the proper phase-locked lags among all four cells for the given gait.

We remark that this design strategy cannot ensure *a priori* to obtain all the desired gaits, as pointed out in Section IV; therefore, the behavior of the resulting CPG must be always checked *a posteriori* (step 4). Moreover, many parts of the method can be changed, as there exist multiple ways to realize this process. For instance, the choice of the interpolation strategy or of the reference cell.

Finally, we remark that this strategy is suitable for networks with a limited number of cells. By construction, the principal limitation of our method is that we have to verify that the CPG under design keeps the features learned during the previous steps. For CPGs with large cell numbers, it would become increasingly difficult to obtain through our local strategy functions of  $\alpha$  that well capture the behavior of the network. On the other hand, the prime focus of our approach is designing simple CPGs with the basic functional mechanisms underlying locomotion. Therefore, from this standpoint, the fact that our

method works well for simple CPGs is hardly a limitation but a gain.

#### IV. ROBUSTNESS OF THE DESIGN STRATEGY

This section is a showcase of the results obtained for four further CPGs, with the same wiring diagram in Fig. 3, that are made of different cell and synapse models, see Appendices A and B. Although preserving the network topology, we test different synapse and cell models to verify the robustness of the proposed design strategy.

Each CPG is symbolically labeled as  $[x/y]$  with the employed cell/synapse models (see Appendices A and B). In the first two CPGs with the tandems:  $[B/\beta]$  and  $[C/\beta]$ , we consider two alternative cell models, whereas in the other two CPGs, namely,  $[A/\gamma]$  and  $[A/\delta]$ , we examine how two alternative synaptic models can alter the network dynamics. We remark that the parameters of the dynamical synapse model  $\delta$  are chosen in order to ensure fast dynamics, according to Section III-B. To build these CPGs, we follow the checklist described in Section III-D.

As pointed out in Section III-D, our method to set the landmarks and obtain the required PWL functions does not need a high resolution of the bifurcation diagram. It is sufficient to get a rough idea of the color regions. This is, of course, an advantage, from a computational standpoint, and for this reason, the bifurcation diagrams in this section are quite rough.

*Step 1:* The starting point is the calibration of the cell model. Fig. 9 shows a 1-D bifurcation sweep (on an array of 100 uniformly spaced  $D_1$  samples) of the frequency  $f$  and DC that are plotted against  $D_1$  in models B and C. As far as model C is concerned [Fig. 9(b)], variations of  $D_1$  properly influence both the frequency (top) and the DC (middle) of every cell of the network. However, in model B [Fig. 9(a)], the ranges of the frequency and DC do not cover all the values necessary for the CPG-network to produce all four gaits (see Table I). Therefore,  $[B/\beta]$ -CPG can only produce walk (left light green region) and trot [central light-blue region in Fig. 9(a)]. For this reason, we select the PWL function  $D_1(\alpha)$  only for  $\alpha \in [0, 0.5]$ . On the contrary, model C can well generate all the required  $f$  and DC values when we choose the PWL function  $D_1(\alpha)$  as described in Section III-D. The obtained results are coherent with the model complexity and biological plausibility levels. We remark that the parameters of model C are set in order to have bursting activity, instead of spiking as in the other cases.

*Step 2:* Bifurcation diagram in Fig. 10 is the  $(\alpha, \Delta D)$ -parameter sweep of  $\Delta_{14}$  on a grid of  $100 \times 100$  parameter values. The white spaces correspond to the regions where cells 1 and/or 3 become quiescent. Therefore, we focus on the colored regions. All the proposed CPGs are able to generate for each value of  $\alpha$  an asymptotic phase lag  $\Delta_{14}$  in the range  $[0.25, 0.65]$ , so cells 1 and 4 can regulate front and hind limbs to move with a plethora of phase lags, thus producing different gaits. To select the landmarks and the PWL functions in Fig. 10, we employ the strategy described in Section III-D. We remark once more that for CPG  $[B/\beta]$  [see Fig. 10(a)], we compute the diagram only for

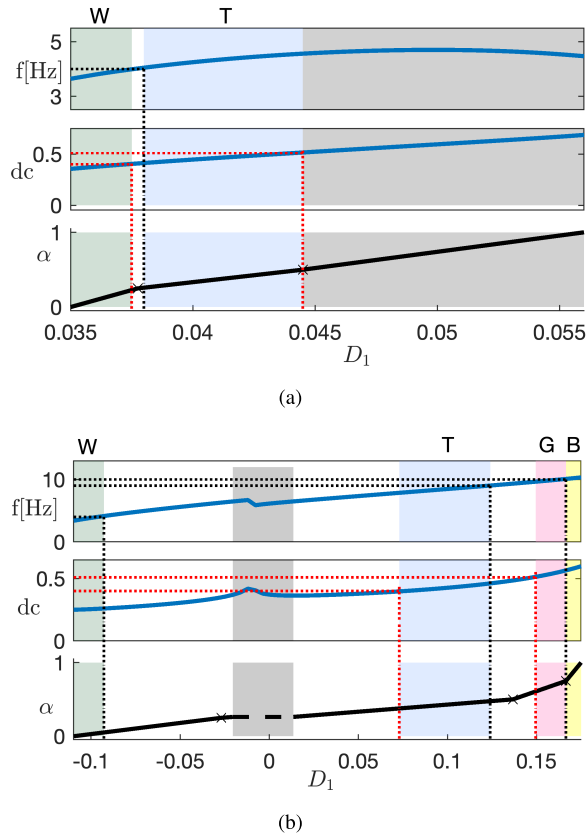


Fig. 9. Step 1. Frequency  $f$  (top), DC (middle) plotted against  $D_1$  for cell models (a) B and (b) C. Dotted lines: boundaries for each gait (see Table I). Crosses: landmarks to define and calibrate the functions  $D_1(\alpha)$ , whose inverse functions  $\alpha(D_1)$  are shown in the bottom. Gray regions do not correspond to any mouse gait, while white regions of  $f$  and DC correspond to multiple stable gaits.

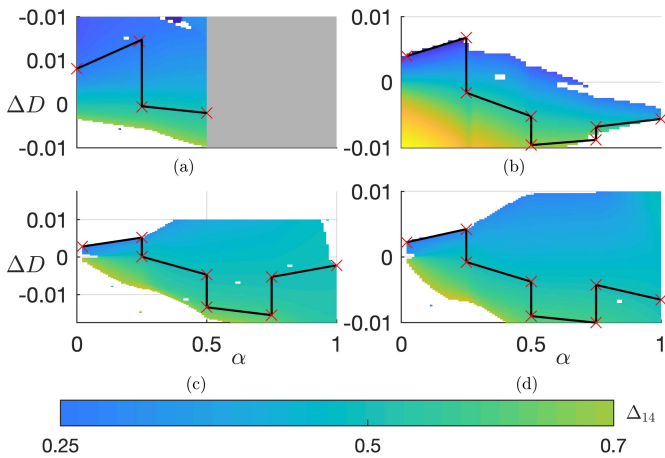


Fig. 10. Step 2. Bifurcation diagrams in the  $(\alpha, \Delta D)$ -parameter plane for cell-synapse models. (a)  $[B/\beta]$ , (b)  $[C/\beta]$ , (c)  $[A/\gamma]$ , and (d)  $[A/\delta]$ . White spaces are composed of parameter pairs corresponding to quiescent cells. Red crosses: landmarks to define and calibrate the function  $\Delta D(\alpha)$  (PWL black graph). Gray region in (a) denotes a not feasible interval of  $\alpha$ -values.

$\alpha \in [0, 0.5]$  because this CPG can only produce walk and trot gaits.

*Step 3:* The bifurcation diagram depicted in Fig. 11 is the biparametric sweep on a grid of  $50 \times 50$   $(\alpha, g^{\text{ex}})$  pairs.

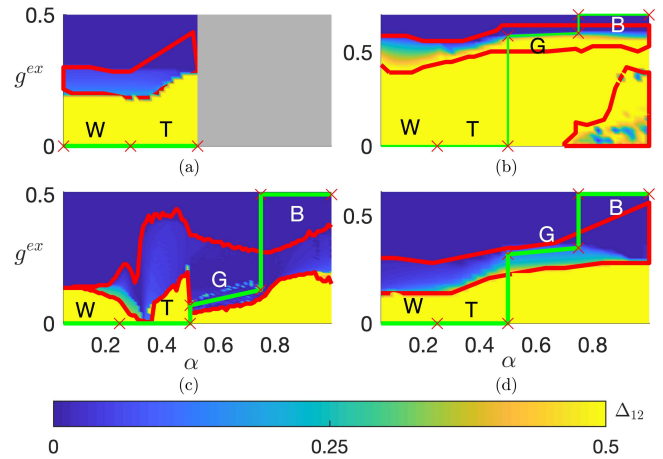


Fig. 11. Step 3. Bifurcation diagrams in the  $(\alpha, g^{\text{ex}})$ -parameter plane for cell-synapse CPG tandems: (a)  $[B/\beta]$ , (b)  $[C/\beta]$ , (c)  $[A/\gamma]$ , and (d)  $[A/\delta]$ . Red crosses: landmarks to define the function  $g^{\text{ex}}(\alpha)$  (PWL green graph). Red lines: pitchfork bifurcations bounding the bistability regions.

One can observe a similarity in all panels, particularly in the upper part (dark blue region) where the cells synchronize in phase with  $\Delta_{12} = 0$ , whereas in the lower part (yellow region), they synchronize in antiphase with  $\Delta_{12} = 0.5$ . The red lines mark pitchfork bifurcations bounding bistability regions in the diagram. Overall, we can obtain any phase lag,  $\Delta_{12}$  ranging from 0 to 1. All CPG circuits, except for the  $[A/\gamma]$  tandem, can generate the necessary phase-lags  $\Delta_{12}$ . Specifically, the  $[A/\gamma]$ -CPG does not yield  $\Delta_{12} = 0.5$  (as a unique solution) when  $\alpha \in [0.3, 0.4]$ , and therefore, it does not produce the trot gait. This limitation is due to the synapse  $\gamma$ -model, which is not continuous. On the contrary, the more realistic  $\delta$ -model provides the results shown in Fig. 11(d), that are coherent with those shown in Fig. 6. We reiterate that the methodology to define the PWL functions  $g^{\text{ex}}(\alpha)$  (green lines in Fig. 11) is the same as in Section III-D.

*Step 4:* The four panels in Fig. 12 show the desired (dashed lines) phase-locked lags  $\Delta_{1i}$  overlaid with the simulated ones (solid lines) for the four CPG models. The  $[C/\beta]$ - and  $[A/\delta]$ -CPGs can generate all four gaits within the whole range of  $\alpha$  values. As expected,  $[B/\beta]$ -CPG generates only walk and trot gaits because, as described in Step 1, it is out of reach of the frequency and the DC associated with gallop and bound.  $[A/\gamma]$ -CPG, as described in Step 3, does not generate trot as a unique gait within  $\alpha \in [0.3, 0.4]$  [gray region on the left in Fig. 12(a)]. Moreover, this CPG cannot generate gallop, probably due to the excessive roughness of the synapse model.

All CPGs switch smoothly between gaits. In particular, for  $[C/\beta]$ -CPG, which is the only one containing bursting cells, Fig. 13 shows the time evolution of the membrane voltages  $V_i$  and of the phase-lags  $\Delta_{1i}$  when  $\alpha$  is increased smoothly across the edge between: walk and trot (top), trot and gallop (middle), and gallop and bound (bottom) regions.

The results obtained on the complete CPGs are indicative that their dynamics are not strongly dependent on the synapse or/and cell models employed, provided that they are not too oversimplified.

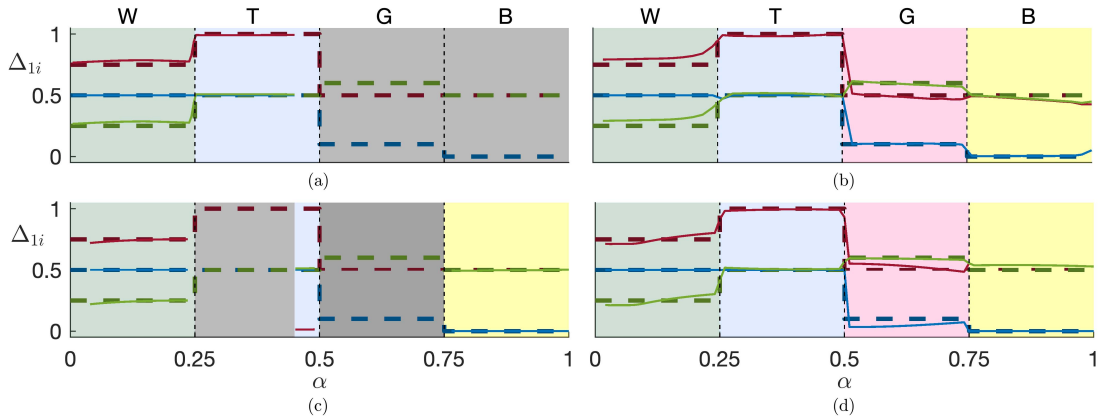


Fig. 12. Step 4. The desired (dashed lines) and simulated (solid lines) phase-locked lags  $\Delta_{1i}$ ,  $i = 2$  (blue),  $i = 3$  (red) and  $i = 4$  (green) for cell-synapse model tandems. (a)  $[B/\beta]$ , (b)  $[C/\beta]$ , (c)  $[A/\gamma]$ , and (d)  $[A/\delta]$ . The bifurcation diagram is subdivided into four regions corresponding to the desired gaits: walk, trot, gallop and bound. Gray regions are  $\alpha$ -intervals without stable gaits.

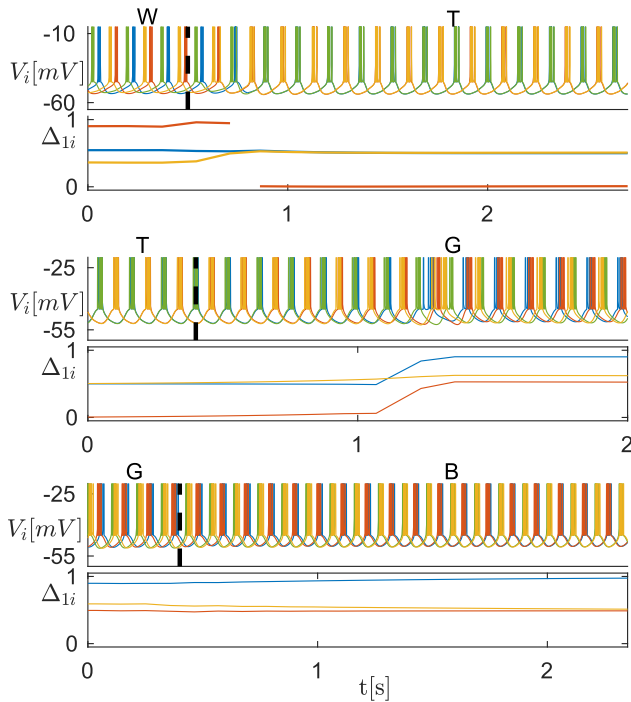


Fig. 13. Time-plots of the “membrane potentials”  $V_i$ , and phase-lags  $\Delta_{1i}$ , at gait transitions for  $[C/\beta]$ -CPG: from walk to trot (top), from trot to gallop (middle), and from gallop to bound (bottom). The colors of the  $V_i(t)$  curves are matched with those of the corresponding cells in Fig. 3.

## V. CONCLUSION

We proposed a four-step method for the design of synthetic CPGs able to produce a prescribed set of gaits. Our strategy requires that both cells and synapses meet some generic assumptions: each cell has to possess the PIR mechanism and each synapse must be fast, even if it is delayed. In the absence of the PIR mechanism,  $\Delta_{14}$  would span smaller ranges, thus making the dynamics of the CPG less controllable. In turn, this makes it more difficult to stably realize all the prescribed

gaits. Moreover, obtaining the small phase lags needed to produce some gaits is more problematic with slow synapses [20]. The “richness” of the cell models plays another key role: more accurate and adequate models allow one to accomplish the design priorities more easily. For instance, with model B (simpler than model A), the occurrence of two out of the four prescribed gaits happened to be unmanageable.

Our method can be applied either to reduce a biological CPG or to an assigned CPG topology. Generally, with our method, one can reduce any biological CPG to its synthetic surrogate with similar rhythm generation. Alternative reduction strategies can be further developed by resorting to cluster synchronization methods [39], for instance, provided that they are applicable for heterogeneous networks. Other methods, particularly, those based on the mathematical theory of groupoids, aim to find the minimum-size network architecture producing formal phase-locking patterns [40], regardless of stability and particularities of cell and synapse models. For instance, the minimum-size CPG model for quadrupeds requires eight cells and overall six underlying assumptions [41]. Note that gait transitions, often depending on the specifics of cell and synapse types, are typically ignored or neglected *a priori* by these methods. Other approaches for managing gait transitions are discussed in [42].

The principal limitation of our method is that it relies on the local properties of the CPG at each step. Although this deterministic approach works well for simple CPGs, it may become less manageable for larger networks that are expected to produce more complex multiphase dynamics. On the other hand, one of the main aims of our approach is the development of the design principles for simple CPGs, with the focus on the basic functional mechanisms underlying locomotion.

The main applications of our reduced models (in addition to their contribution to understanding the basic mechanisms producing locomotion in living beings) are in the field of robotics [42], [43] and rehabilitation [44], [45].

APPENDIX A  
 CELL MODELS

## A. A-Model

This model, used in [30], is described by the following equations:

$$\begin{aligned}
 C \frac{dV_i}{dt} &= 7 - I_{Na} - I_L - g_D D_i(\alpha)(V_i - E_{ex}) + I_{syn}^{(i)} \\
 \tau \frac{dh_i}{dt} &= h_\infty - h_i, \quad I_L = g_L(V_i - E_L) \\
 I_{Na} &= g_{Na} m h_i (V_i - E_{Na}), \quad m = \left(1 + e^{\frac{V_i - V_m}{k_m}}\right)^{-1} \\
 h_\infty &= \left(1 + e^{\frac{V_i - V_h}{k_h}}\right)^{-1}, \quad \tau = \tau_0 + \frac{\tau_M - \tau_0}{\cosh\left(\frac{V_i - V_\tau}{k_\tau}\right)}
 \end{aligned} \quad (4)$$

where  $C = 10$  pF,  $g_L = 4.5$  nS,  $E_L = -62.5$  mV,  $g_{Na} = 4.5$  nS,  $E_{Na} = 50$  mV,  $V_m = -40$  mV,  $k_m = -6$  mV,  $V_h = -45$  mV,  $k_h = 4$  mV,  $\tau_0 = 80$  ms,  $\tau_M = 160$  ms,  $V_\tau = -35$  mV,  $k_\tau = 15$  mV, and  $g_D = 10$  nS.

## B. B-Model

This generalized FitzHugh–Nagumo model proposed in [8] is described by the following equations:

$$\begin{cases} \tau \dot{V}_i = V_i - V_i^3 - x_i + I - g_D D_i(\alpha)(V_i - E_{ex}) + I_{syn}^{(i)} \\ \dot{x}_i = \varepsilon(X_\infty - X_i), \quad X_\infty = \frac{1}{1 + e^{-4V_i}} \end{cases} \quad (5)$$

where  $\tau = 6.75$  ms,  $I = 0$ ,  $g_D = 10$ ,  $E_{ex} = 1.15$ , and  $\varepsilon = 0.15$  ms<sup>-1</sup>.

## C. C-Model

This adaptive exponential integrate-&fire model [31] is described by the following equations:

$$\begin{aligned}
 C \frac{dV_i}{dt} &= -g_L(V_i - E_L) + g_e e^{\frac{V_i - V_T}{\Delta T}} + \\
 &\quad -g_D D_i(\alpha)(V_i - E_{ex}) - u_i + I + I_{syn}^{(i)} \\
 \tau_w \frac{du_i}{dt} &= a(V_i - E_L) - u_i
 \end{aligned} \quad (6)$$

subject to the reset rule

$$\text{if } V_i > 20, \text{ then } \begin{cases} V_i \leftarrow V_r \\ u_i \leftarrow u_i + b \end{cases} \quad (7)$$

where  $C = 501.8$  pF,  $g_L = 30$  nS,  $E_L = -70.6$  mV,  $V_T = -50.4$  mV,  $\Delta T = 2$  mV,  $E_{ex} = 20$  mV,  $\tau_w = 71.4$  ms,  $a = 4$  nS,  $b = 100$  pA,  $V_r = -45$  mV,  $I = 800$  pA,  $g_e = 25$  pA, and  $g_D = 10$  nS.

 APPENDIX B  
 SYNAPSE MODELS

 A.  $\beta$ -Model

Model  $\beta$  follows the FTM paradigm [32]:  $A(V) = (1/(1 + e^{-\nu_\beta(V - \theta_\beta)}))$ .

 TABLE II  
 SYNAPSES STRENGTH

Parameters	values	Parameters	values
$g_{12}^{in}, g_{12}^{in}, g_{34}^{in}, g_{43}^{in}$	$g_0^{in} \cdot 0.2984$	$g_{14}^{in}, g_{23}^{in}$	$g_0^{in} \cdot 0.1241$
$g_{12}^{di}, g_{12}^{di}, g_{34}^{di}, g_{43}^{di}$	$g_0^{di} \cdot 0.0221$	$g_{32}^{in}, g_{41}^{in}$	$g_0^{in} \cdot 0.0532$
$g_{12}^{ex}, g_{12}^{ex}$	$g_{12}^{ex}(\alpha)$	$g_{34}^{ex}, g_{43}^{ex}$	$g_{34}^{ex}(\alpha)$

TABLE III

SYNAPSES PARAMETERS FOR ALL THE EMPLOYED CELL MODELS

Synapse	Parameters	model A	model B	model C
$\beta$ -model	$\theta_\beta$	-30mV	0	-48.5mV
	$\nu_\beta$	$0.3\text{mV}^{-1}$	100	$1.5\text{mV}^{-1}$
$\gamma$ -model	$\theta_\gamma$	-39mV	-	-
$\delta$ -model	$\theta_\delta$	-30mV		
	$\nu_\delta$	$0.3\text{mV}^{-1}$		
	a	$1\text{ms}^{-1}$	-	-
	b	$0.1\text{ms}^{-1}$		
all models	$E_{in}$	-75mV	-1.15	-75mV
	$E_{ex}$	-10mv	1.15	20mV
	$g_0^{in}$	1nS	1	5nS
	$g_0^{di}$	1nS	1	1nS
	$g_0^{ex}$			

 B.  $\gamma$ -Model

In this model, the activation (nonstate-dependent) is  $A(V) = H(V - \theta_\gamma)$ , where  $H(\cdot)$  is the Heaviside function.

 C.  $\delta$ -Model

This dynamical so-called  $\alpha$ -synapse model [33], [46] has a state equation given by

$$\dot{s} = a(1 - s) \frac{1}{1 + e^{-\nu_\delta(V - \theta_\delta)}} - b s \quad (8)$$

with the activation function given by  $A(V, s) = (a + b/a)s$ .

## D. Synapse Parameters

The synapse strengths are listed in Table II, whereas the values of the other parameters are listed in Table III.

## ACKNOWLEDGMENT

A. L. Shilnikov would like to thank the GSU Brain and Behaviors Initiative for the Fellowship and Pilot Grant support.

## REFERENCES

- [1] A. J. Ijspeert, "Central pattern generators for locomotion control in animals and robots: A review," *Neural Netw.*, vol. 21, no. 4, pp. 642–653, 2008.
- [2] A. Kozlov, M. Huss, A. Lansner, J. H. Koteleski, and S. Grillner, "Simple cellular and network control principles govern complex patterns of motor behavior," *Proc. Nat. Acad. Sci. USA*, vol. 106, no. 47, pp. 20027–20032, 2009.
- [3] O. Kiehn, "Decoding the organization of spinal circuits that control locomotion," *Nat. Rev. Neurosci.*, vol. 17, pp. 224–238, Mar. 2016.
- [4] J. Yu, M. Tan, J. Chen, and J. Zhang, "A survey on CPG-inspired control models and system implementation," *IEEE Trans. Neural Netw. Learn. Syst.*, vol. 25, no. 3, pp. 441–456, Mar. 2014.
- [5] L. P. Shilnikov, A. L. Shilnikov, D. V. Turaev, and L. O. Chua, *Methods Of Qualitative Theory in Nonlinear Dynamics. Part I*, vol. 5. Singapore: World Scientific, 1998.

- [6] L. P. Shilnikov, A. L. Shilnikov, D. V. Turaev, and L. O. Chua, *Methods Of Qualitative Theory in Nonlinear Dynamics. Part II*, vol. 5. Singapore: World Scientific, 2001.
- [7] J. Wojcik, J. Schwabedal, R. Clewley, and A. L. Shilnikov, "Key bifurcations of bursting polyrhythms in 3-cell central pattern generators," *PLoS ONE*, vol. 9, no. 4, 2014, Art. no. e92918.
- [8] J. T. C. Schwabedal, D. E. Knapper, and A. L. Shilnikov, "Qualitative and quantitative stability analysis of penta-rhythmic circuits," *Nonlinearity*, vol. 29, no. 12, pp. 3647–3676, 2016.
- [9] Z. Aminzare, V. Srivastava, and P. Holmes, "Gait transitions in a phase oscillator model of an insect central pattern generator," *SIAM J. Appl. Dyn. Syst.*, vol. 17, no. 1, pp. 626–671, 2018.
- [10] A. Sobinov and S. Yakovenko, "Model of a bilateral Brown-type central pattern generator for symmetric and asymmetric locomotion," *J. Neurophysiol.*, vol. 119, no. 3, pp. 1071–1083, 2017.
- [11] P. Capelli, C. Pivetta, M. S. Esposito, and S. Arber, "Locomotor speed control circuits in the caudal brainstem," *Nature*, vol. 551, no. 7680, pp. 373–377, 2017.
- [12] V. Caggiano *et al.*, "Midbrain circuits that set locomotor speed and gait selection," *Nature*, vol. 553, pp. 455–460, Jan. 2018.
- [13] J. Ausborn, N. A. Shevtsova, V. Caggiano, S. M. Danner, and I. A. Rybak, "Computational modeling of brainstem circuits controlling locomotor frequency and gait," *eLIFE*, vol. 8, Jan. 2019, Art. no. e43587.
- [14] M. Lodi, A. Shilnikov, and M. Storace, "Design of minimal synthetic circuits with sensory feedback for quadruped locomotion," in *Proc. IEEE Int. Symp. Circuits Syst. (ISCAS)*, May 2018, pp. 1–5.
- [15] M. Lodi, A. Shilnikov, and M. Storace, "CEPAGE: A toolbox for central pattern generator analysis," in *Proc. IEEE Int. Symp. Circuits Syst. (ISCAS)*, May 2017, pp. 1–4.
- [16] M. Lodi, A. Shilnikov, and M. Storace, "Design of synthetic central pattern generators producing desired quadruped gaits," *IEEE Trans. Circuits Syst. I, Reg. Papers*, vol. 65, no. 3, pp. 1028–1039, Mar. 2018.
- [17] D. A. McCreary and I. A. Rybak, "Organization of mammalian locomotor rhythm and pattern generation," *Brain Res. Rev.*, vol. 57, no. 1, pp. 134–146, 2008.
- [18] N. S. Szczecinski, A. J. Hunt, and R. D. Quinn, "A functional sub-network approach to designing synthetic nervous systems that control legged robot locomotion," *Frontiers Neurobot.*, vol. 11, p. 37, Aug. 2017.
- [19] X.-J. Wang and J. Rinzel, "Alternating and synchronous rhythms in reciprocally inhibitory model neurons," *Neural Comput.*, vol. 4, no. 1, pp. 84–97, 1992.
- [20] E. Marder and R. L. Calabrese, "Principles of rhythmic motor pattern generation," *Physiol. Rev.*, vol. 76, no. 3, pp. 687–717, 1996.
- [21] D. Owaki and A. Ishiguro, "A quadruped robot exhibiting spontaneous gait transitions from walking to trotting to galloping," *Sci. Rep.*, vol. 7, no. 1, p. 277, 2017.
- [22] J. Ausborn, A. C. Snyder, N. A. Shevtsova, I. A. Rybak, and J. E. Rubin, "State-dependent rhythmogenesis and frequency control in a half-center locomotor CPG," *J. Neurophysiol.*, vol. 119, no. 1, pp. 96–117, 2017.
- [23] J. Wojcik, R. Clewley, and A. Shilnikov, "Order parameter for bursting polyrhythms in multifunctional central pattern generators," *Phys. Rev. E, Stat. Phys. Plasmas Fluids Relat. Interdiscip. Top.*, vol. 83, May 2011, Art. no. 056209.
- [24] L. Zhao and A. Nogaret, "Experimental observation of multistability and dynamic attractors in silicon central pattern generators," *Phys. Rev. E, Stat. Phys. Plasmas Fluids Relat. Interdiscip. Top.*, vol. 92, no. 5, 2015, Art. no. 052910.
- [25] S. Jalil, D. Allen, J. Youker, and A. Shilnikov, "Toward robust phase-locking in Melibe swim central pattern generator models," *Chaos*, vol. 23, no. 4, 2013, Art. no. 046105.
- [26] R. Barrio, M. Rodríguez, S. Serrano, and A. Shilnikov, "Mechanism of quasi-periodic lag jitter in bursting rhythms by a neuronal network," *Europhys. Lett.*, vol. 112, no. 3, 2015, Art. no. 38002.
- [27] C. Bellardita and O. Kiehn, "Phenotypic characterization of speed-associated gait changes in mice reveals modular organization of locomotor networks," *Current Biol.*, vol. 25, no. 11, pp. 1426–1436, 2015.
- [28] M. Lemieux, N. Jossset, M. Roussel, S. Couraud, and F. Bretzner, "Speed-dependent modulation of the locomotor behavior in adult mice reveals attractor and transitional gaits," *Frontiers Neurosci.*, vol. 10, p. 42, Feb. 2016.
- [29] D. H. Perkel and B. Mulloney, "Motor pattern production in reciprocally inhibitory neurons exhibiting postinhibitory rebound," *Science*, vol. 185, no. 4146, pp. 181–183, 1974.
- [30] S. M. Danner, S. D. Wilshin, N. A. Shevtsova, and I. A. Rybak, "Central control of interlimb coordination and speed-dependent gait expression in quadrupeds," *J. Physiol.*, vol. 594, no. 23, pp. 6947–6967, 2016.
- [31] R. Brette and W. Gerstner, "Adaptive exponential integrate-and-fire model as an effective description of neuronal activity," *J. Neurophysiol.*, vol. 94, no. 5, pp. 3637–3642, 2005.
- [32] D. Somers and N. Kopell, "Rapid synchronization through fast threshold modulation," *Biol. Cybern.*, vol. 68, no. 5, pp. 393–407, 1993.
- [33] C. Van Vreeswijk, L. F. Abbott, and G. B. Ermentrout, "When inhibition not excitation synchronizes neural firing," *J. Comput. Neurosci.*, vol. 1, no. 4, pp. 313–321, 1994.
- [34] M. Ren, Y. Yoshimura, N. Takada, S. Horibe, and Y. Komatsu, "Specialized inhibitory synaptic actions between nearby neocortical pyramidal neurons," *Science*, vol. 316, no. 5825, pp. 758–761, 2007.
- [35] B. W. Connors and S. J. Cruikshank, "Bypassing interneurons: Inhibition in neocortex," *Nature NeuroSci.*, vol. 10, no. 7, pp. 808–810, 2007.
- [36] A. Sakurai and P. S. Katz, "The central pattern generator underlying swimming in *Dendronotus iris*: A simple half-center network oscillator with a twist," *J. Neurophysiol.*, vol. 116, no. 4, pp. 1728–1742, 2016.
- [37] A. Sakurai, C. A. Gunaratne, and P. S. Katz, "Two interconnected kernels of reciprocally inhibitory interneurons underlie alternating left-right swim motor pattern generation in the mollusk *Melibe leonina*," *J. Neurophysiol.*, vol. 112, no. 6, pp. 1317–1328, 2014.
- [38] A. Sakurai and P. S. Katz, "Phylogenetic and individual variation in gastropod central pattern generators," *J. Comparative Physiol. A*, vol. 201, no. 9, pp. 829–839, 2015.
- [39] A. B. Siddique, L. Pecora, J. D. Hart, and F. Sorrentino, "Symmetry- and input-cluster synchronization in networks," *Phys. Rev. E, Stat. Phys. Plasmas Fluids Relat. Interdiscip. Top.*, vol. 97, no. 4, 2018, Art. no. 042217.
- [40] M. Golubitsky and I. Stewart, "Rigid patterns of synchrony for equilibria and periodic cycles in network dynamics," *Chaos*, vol. 26, no. 9, 2016, Art. no. 094803.
- [41] M. Golubitsky, I. Stewart, P.-L. Buono, and J. J. Collins, "Symmetry in locomotor central pattern generators and animal gaits," *Nature*, vol. 401, no. 6754, pp. 693–695, 1999.
- [42] J. Yu, Z. Wu, M. Wang, and M. Tan, "CPG network optimization for a biomimetic robotic fish via PSO," *IEEE Trans. Neural Netw. Learn. Syst.*, vol. 27, no. 9, pp. 1962–1968, Sep. 2016.
- [43] Y. Hu, J. Liang, and T. Wang, "Parameter synthesis of coupled nonlinear oscillators for CPG-based robotic locomotion," *IEEE Trans. Ind. Electron.*, vol. 61, no. 11, pp. 6183–6191, Nov. 2014.
- [44] K. A. Mazurek, B. J. Holinski, D. G. Everaert, V. K. Mushahwar, and R. Etienne-Cummings, "A mixed-signal VLSI system for producing temporally adapting intraspinal microstimulation patterns for locomotion," *IEEE Trans. Biomed. Circuits Syst.*, vol. 10, no. 4, pp. 902–911, Aug. 2016.
- [45] J. A. Bamford, R. M. Lebel, K. Parseyan, and V. K. Mushahwar, "The fabrication, implantation, and stability of intraspinal microwire arrays in the spinal cord of cat and rat," *IEEE Trans. Neural Syst. Rehabil. Eng.*, vol. 25, no. 3, pp. 287–296, Mar. 2017.
- [46] S. Jalil, I. Belykh, and A. Shilnikov, "Spikes matter for phase-locked bursting in inhibitory neurons," *Phys. Rev. E, Stat. Phys. Plasmas Fluids Relat. Interdiscip. Top.*, vol. 85, Mar. 2012, Art. no. 036214.



**Matteo Lodi** was born in Genoa, Italy, in 1991. He received the Laurea (M.Sc.) degree (*Summa Cum Laude*) in electronic engineering from the University of Genoa, Genoa, in 2015, where he is currently pursuing the Ph.D. degree in electrical engineering.

He was a Visitor with the NEURDS-Lab, Georgia State University, Atlanta, GA, USA, in 2016, and BioRob Lab, EPFL, Lausanne, Switzerland, in 2017. His current research interests include modeling of nonlinear systems (hysteresis and networks of biological neurons) and bifurcation analysis.



**Andrey Shilnikov** was born in Nizhny Novgorod, Russia, in 1962. He received the M.S. degree in mathematics and physics and the Ph.D. degree in differential equations including mathematical physics from the University of Nizhny Novgorod, Nizhny Novgorod, in 1984 and 1990, respectively.

He was a Post-Doctoral Fellow with UC Berkeley, Berkeley, CA, USA, from 1993 to 1994. He was a Royal Society Post-Doctoral Fellow with Cambridge University, Cambridge, CB, U.K., from 1994 to 1995. In 2000, he joined GSU, Atlanta, GA, USA.

He held visiting positions at UC Berkeley, Georgia Institute of Technology, Atlanta, and Cornell University, Ithaca, NY, USA. He is currently a Distinguished University Professor with the Department of Mathematics and Statistics, Neuroscience Institute, GSU. He has authored more than 100 scholarly publications, including advanced textbooks on dynamical systems. His current research interests include dynamical systems and mathematical neuroscience.

Dr. Shilnikov serves on Editorial Boards for the *Journal of Mathematical Neuroscience*, the *Journal of Discontinuity, Nonlinearity and Complexity*, and the *Journal of Frontiers of Applied Mathematics*.



**Marco Storace** (M'01–SM'14) was born in Genoa, Italy, in 1969. He received the Laurea (M.Sc.) degree (*Summa Cum Laude*) and the Ph.D. degree in electronic engineering from the University of Genoa, Genoa, in March 1994 and April 1998, respectively.

Since 2011, he has been a Full Professor with the University of Genoa. He was a Visitor with EPFL, Lausanne, Switzerland, in 1998 and 2002. He has authored or coauthored more than 140 scientific articles, more than half of which have been published in international journals. His current research interests

include nonlinear circuit theory and applications, with emphasis on (circuit) models of nonlinear systems (e.g., hysteresis and biological neurons), methods for the piecewise linear approximation of nonlinear systems, bifurcation analysis, and nonlinear dynamics.

Dr. Storace is a member of the IEEE Technical Committee on Nonlinear Circuits and Systems (TC-NCAS). He served as an Associate Editor for the IEEE TRANSACTIONS ON CIRCUITS AND SYSTEMS—II: EXPRESS BRIEFS from 2008 to 2009.